Dynamics of Atmospheres and Oceans 109 (2025) 101520

Contents lists available at ScienceDirect

Dynamics of Atmospheres and Oceans

journal homepage: www.elsevier.com/locate/dynatmoce

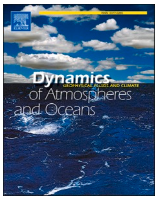

The regional coupled ocean-atmosphere model simulation over Eastern Tropical Africa

Vasubandhu Misra[a,b,*], C.B. Jayasankar[b]

[a] Department of Earth, Ocean and Atmospheric Science, Florida State University, Tallahassee, FL, USA
[b] Center for Ocean-Atmospheric Prediction Studies, Florida State University, Tallahassee, FL, USA

ARTICLE INFO

Keywords:
Regional climate model
Air-sea interaction
Diurnal variability
Intra-seasonal variability

ABSTRACT

In this study we examine a 25-year simulation of a Regional Coupled Ocean-Atmosphere Model (RCOM) forced by global atmospheric and ocean reanalysis at the lateral boundaries over eastern equatorial Africa which includes parts of the Great Horn of Africa (GHA). It is a first of its kind use of a RCOM for the region. The model shows several observed features of the regional climate with bimodal peaks in the seasonal cycle interspersed with regions of unimodal peak, significant diurnal and intra-seasonal variations of precipitation especially over Lake Victoria and robust seasonal cycle of the upper western India Ocean. Nonetheless the model shows significant dry bias of seasonal precipitation that is persistent throughout the year, which is also reflected at diurnal and intra-seasonal scales. The mixed layer and thermocline depths are found to be shallower in the model simulation suggesting a far more stratified upper western Indian Ocean than the observations indicate.

1. Introduction

The regional domain covered in this study is part of the Great Horn of Africa (GHA) which includes parts of southern Somalia, South Sudan, Ethiopia, Kenya, Democratic Republic of Congo (DRC), Tanzania, Uganda, Rwanda, and Burundi as shown in Fig. 1. The region is well known for a complex seasonal cycle of the hydroclimate with some of these countries exhibiting bi-modal peaks in rainfall (e.g., Kenya, Uganda, Somalia) and other parts exhibiting unimodal peak (e.g., Tanzania, South Sudan) of the seasonal cycle (Nicholson, 1996; Herrmann and Mohr, 2011; Cook and Vizy, 2013; Lyon, 2014; Yang et al., 2015; Palmer et al., 2023). Furthermore, GHA exhibits a relatively drier climate compared to much of the continental tropical areas at the same latitude (Nicholson, 2011; Yang et al., 2015).

In most of GHA, much of the annual rain appears in the transition seasons of boreal fall and spring seasons with exceptions over Tanzania, DRC, and South Sudan. Some of these hydroclimatic features of GHA have been attributed to the complex topography of the region (Nicholson, 1996; Lyon, 2014). For instance, Bryson and Kuhn (1961) indicate that subsidence prevails in GHA owing to the frictional contrast between the low-level monsoonal flow along the shore and the adjacent coastal ocean, which then results with the transition seasons of boreal fall and spring seasons to have the highest rainfall when the monsoonal flow is weak. Similarly, the equatorward easterlies as part of the return flow of the local meridional overturning circulation (local Hadley Cell) is associated with subsiding air, which becomes weaker during the transition seasons forcing the rainfall to be highest in the region. Nicholson (1996) also suggests that shallow moist air flow constricted by local topography, subsidence induced at the exit of low-level jets like the

---

* Corresponding author at: Department of Earth, Ocean and Atmospheric Science, Florida State University, Tallahassee, FL, USA.
E-mail address: vmisra@fsu.edu (V. Misra).

https://doi.org/10.1016/j.dynatmoce.2024.101520
Received 19 September 2024; Received in revised form 15 November 2024; Accepted 29 November 2024

Turkana Jet, and leeward rain shadow areas of the East African Highlands and Ethiopian Highlands forcing subsidence, while the Great Rift Valley blocking the moist air flow from DRC enhance aridity in the region. Furthermore, strong upwelling of the cold water in the coastal oceans off the Somali coast can also enhance aridity in the region.

The regions in GHA that exhibit bimodality in the seasonal cycle are characterized by “long rains” in the boreal spring and “short rains” in the boreal fall season. These names come from the typical duration of the individual rain events being longer and shorter for the spring and fall seasons, respectively (Nicholson, 1996, 2017; Camberlin and Wairoto, 1997; Hastenrath et al., 2011). Although the long rains in the boreal spring season have a greater contribution to the annual rainfall in the region, it is the short rains season that exhibits higher interannual variations (Hastenrath et al., 1993, 2011; Camberlin and Wairoto, 1997; Liu et al., 2020). It is noted that the variation of the short rainy season is strongly dictated by the variations in the western Indian Ocean (Nicholson, 1996; Misra, 2003; Ummenhofer et al., 2009; Liu et al., 2020) while ENSO is found to be more influential in the variations of the long rains season (Nicholson and Entekhabi, 1986; Hastenrath et al., 1993; Black et al., 2003; Funk et al., 2018; Kimutai et al., 2023; Palmer et al., 2023). Several studies suggest that the influence of the western Indian Ocean SST on the GHA short rains is exerted at sub-seasonal timescales (Ummenhofer et al., 2009, Bahaga et al., 2015; Liu et al., 2020).

Simulating the diurnal variations of precipitation over and around Lake Victoria is challenging given its observed complex spatial gradients. For example, Yin and Nicholson (1998) and Camberlin et al. (2017) observe a phase shift in the timing of the maximum rainfall in going from the western to the eastern edges of Lake Victoria. Several high resolution, regional modeling studies indicate that the mesoscale-circulation of the clear afternoon lake breezes and the nighttime land breezes strongly dictate the nocturnal regime of the rainfall over Lake Victoria (Thiery et al., 2015; Sun et al., 2015; Van de Walle et al., 2020). Thus, these studies highlight the importance of regional modeling for the region.

Earlier modeling studies suggest that General Circulation Models (GCMs) do not generally simulate the GHA climate well (Cook and Vizy, 2013; Endris et al., 2013; Ogwang et al., 2016; Dunning et al., 2017). These studies point out that the coarse resolution of the GCMs limits their ability to accurately represent the complex topography and coastline which are important to obtain the regional features of the GHAs regional hydroclimate. On the other hand, Regional Climate Models (RCMs) have demonstrated reasonable success in simulating the hydroclimate and associated regional circulation features of GHA (Cook and Vizy, 2013; Ogwang et al., 2016; Han et al., 2019). In this study, we adopt a regional coupled ocean-atmosphere model to simulate the regional climate of GHA, uniquely configured at 10 km grid resolution for this region. This is a first of its kind configuration of such a high-resolution coupled ocean-atmosphere model for GHA. The aim of this study is to analyze the fidelity of a 25 year simulation from this regional coupled ocean-atmosphere model. In the following section we describe the model, and the verification datasets used. Results are discussed in Section 3 followed by concluding remarks in Section 4.

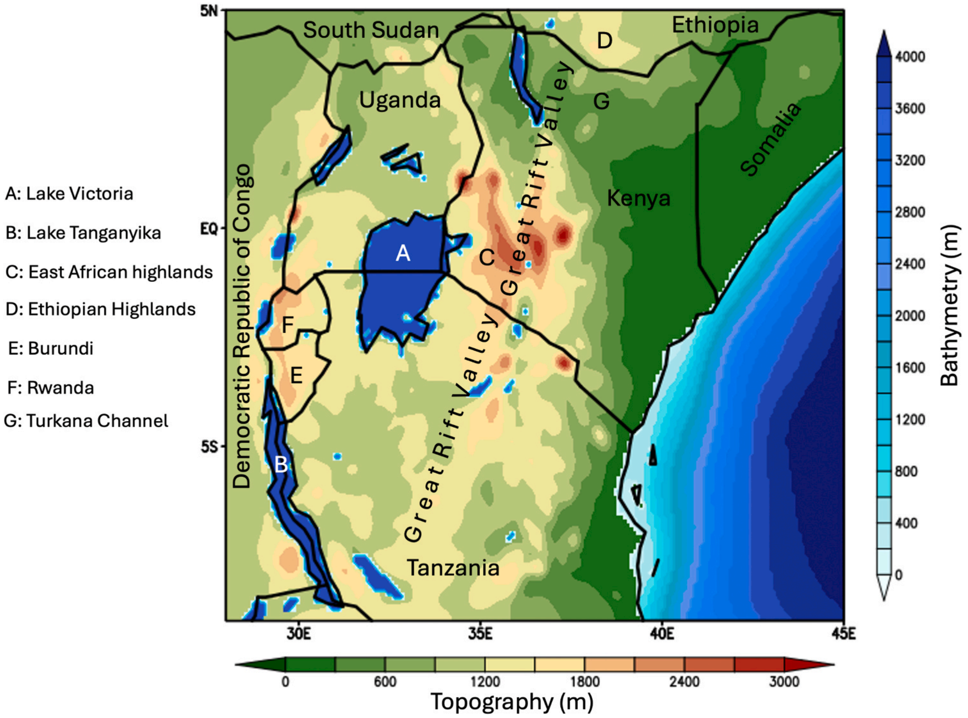

Fig. 1. Illustration of the regional domain with the topography and bathymetry of the Regional Spectral Model-Regional Ocean Modeling System (RSM-ROMS) adopted for the study.

2. Model description

The Regional Spectral Model-Regional Ocean Modeling System (RSM-ROMS) is a widely utilized numerical modeling framework for studying regional atmospheric and oceanic processes (Li and Misra, 2014; Ham et al., 2016; Misra et al., 2022; Misra and Jayasankar, 2022, 2023). This model combines the Regional Spectral Model (RSM) for simulating the atmosphere with the Regional Ocean Modeling System (ROMS) for simulating the oceans on identical grids for the two components of the climate system, typically at 10 km grid spacing. RSM-ROMS provides relatively high-resolution simulations at regional scales, allowing investigations in the coupled ocean-atmosphere framework to provide a holistic understanding of the interconnectedness of these sub-component systems. Its versatility and flexibility have made it a favorable tool for studying climate variability, extreme weather events, and marine ecosystems in diverse geographical regions.

The selection of the physics package detailed in Table 1 has undergone a process of refinement and evolution (Li and Misra, 2014; Ham et al., 2016; Misra et al., 2022; Misra and Jayasankar, 2022, 2023; Jayasankar et al., 2023). Reference datasets such as soil type, vegetation type, and vegetation fraction are made consistent with the land-sea mask from the Global 30 Arc-Second Elevation dataset (Danielson and Gesch, 2011) interpolated to the RSM-ROMS grid. At 10 km grid spacing, ROMS also resolves the various lakes in the domain (Fig. 1). In this study, however, we assigned an abyssal depth to these lakes in ROMS for lack of bathymetry data at this resolution, which we plan to rectify in a future work following (Nyamweya et al., 2016).

ROMS is the regional ocean model component that utilizes a free surface and terrain following a primitive equation framework (Haidvogel et al., 2000; Scheptekin and McWilliams, 2005). This model incorporates 30 vertical stretched terrain (S) levels, with enhanced resolution in the upper ~500 m of the ocean. The horizontal grid employed in ROMS follows the staggered Arakawa-C grid configuration. Various parameterizations are integrated into ROMS which includes the local closure schemes based on the level 2.5 turbulent kinetic energy equations (Mellor and Yamada, 1982) for mixing, a boundary layer formulation rooted in the nonlocal closure scheme (Large et al., 1994), second order biharmonic horizontal diffusion (Ezer et al., 2002) with a generic length-scale parameterization (Umlauf and Burchard, 2003).

For this study, the RSM and the ROMS are integrated on identical spatial grids on a Cartesian coordinate system, with a grid spacing of 10 km. This setup allows for seamless coupling between the two models, eliminating the need for interpolations at their interface and the use of a flux coupler.

Both RSM and ROMS operate within a domain size of 226 grid points in the zonal direction and 168 grid points in the meridional direction. This grid structure ensures a consistent and a direct exchange of atmospheric heat, moisture, radiation, and momentum fluxes, and sea surface temperature (SST) between the two models at a coupling interval of 1 hour without the use of a flux coupler.

3. Experiment design

A 25-year integration is conducted using the RSM-ROMS over the period 1986–2010 centered on the domain shown in Fig. 1. The resolved model topographic and bathymetric features are also illustrated in Fig. 1 for an RSM-ROMS grid spacing of 10 km. At this resolution various topographical and bathymetric features, including coastal shelves, mesoscale mountain ridges, and valleys are depicted reasonably well (Fig. 1). The integration uses the NCEP-DOE reanalysis (R2; Kanamitsu et al., 2002) for lateral boundary conditions of RSM and the Simple Ocean Data Assimilation version 2.2.4 (SODA; Carton and Giese, 2008) for ROMS. Notably, this SODA reanalysis version covers the same 25-year period (1986–2010), which determined the integration period for this study. More recent SODA reanalysis versions are available but cover shorter durations. The R2 reanalysis provides data at a $2.5^\circ \times 2.5^\circ$ grid spacing, while SODA is available at a $0.5^\circ \times 0.5^\circ$ grid resolution. Initial conditions for the RSM atmosphere and land surface are obtained from R2 corresponding to the integration start date. Similarly, initial conditions for ROMS are sourced from SODA, ensuring the ocean is not initialized from a state of rest. This approach mitigates ocean spin-up issues, particularly for the upper ocean (approximately 300–500 m below the surface). These initial conditions are interpolated to the RSM-ROMS grid at its 10 km spacing.

4. Verification data

In this study, the upper air, surface variables and oceanic variables from the RSM-ROMS integration is verified from a variety of observations, as listed in Table 2. There are instances where the validation datasets did not align with the integration period of RSM-ROMS. However, in all instances it is the climatology of the model that is verified. Therefore, we have tried as far as possible to match

Table 1
Outline of the physics package in RSM.

Physical parameterization	Reference
Prognostic clouds	Zhao and Carr (1997)
Landsurface	Ek et al. (2003)
Gravity wave drag	Alpert et al. (1988)
Boundary layer	Hong and Pan (1996)
Longwave radiation	Chou et al. (1999)
Shortwave radiation	Chou and Lee (1996)
Deep convection	Kain and Fritsch (1993)
Shallow convection	Tiedtke (1983)

Table 2
Verification datasets used in the study.

Variable	Source	Purpose	Spatial resolution	Period used in the study
Upper air variables	ERA5 (Hersbach et al., 2019)	Verification of seasonal mean 850hPa winds, precipitable water	0.25° x 0.25°	1986–2010
Rainfall	IMERG v7 (Huffmann et al., 2019)	Verification of seasonal mean, interannual and intraseasonal variations over both land and ocean	0.1° x 0.1°	2001–2023
SST	OISSTv2 (Reynolds et al., 2007)	Verification of seasonal mean SST and rainfall-SST relationship	0.25° x 0.25°	1986–2010
Mixed layer depth	Argo (Holte et al., 2017)	Verification of seasonal mean mixed layer depth	1° x 1°	2000–2020
Depth of the 20°C isotherm in the ocean	SODA reanalysis (Carton and Giese, 2008)	Verification of the depth of the seasonal mean 20°C	0.5° x 0.5°	1986–2010

the number of years to compute the climatology of the verification data to that of the RSM-ROMS integration. It is important to note that we employed linear interpolation of the RSM-ROMS variables to the observed grid when computing differences between them. Otherwise, the fields were plotted on their original grids.

The model validation is conducted on the observation grid i.e., the model output is interpolated to the observation grid, when the bias is computed. In the case of assessing the diurnal variations of the precipitation we isolate the local diurnal harmonic following Dai and Wang (1999). This harmonic analysis involves breaking down a time series into its component parts by decomposing a periodic function into a combination of trigonometric functions such as:

$$P(t) = P_o + \sum_{i=1}^{N/2} \mathbb{R}_i \cos(i\theta - \Phi_i) - - - - - - - - \quad (1)$$

Where, $N, P_o, \mathbb{R}_i, \Phi_i$ are the number of intervals (=24 for hourly), daily mean value of the variable, amplitude, and phase angle of

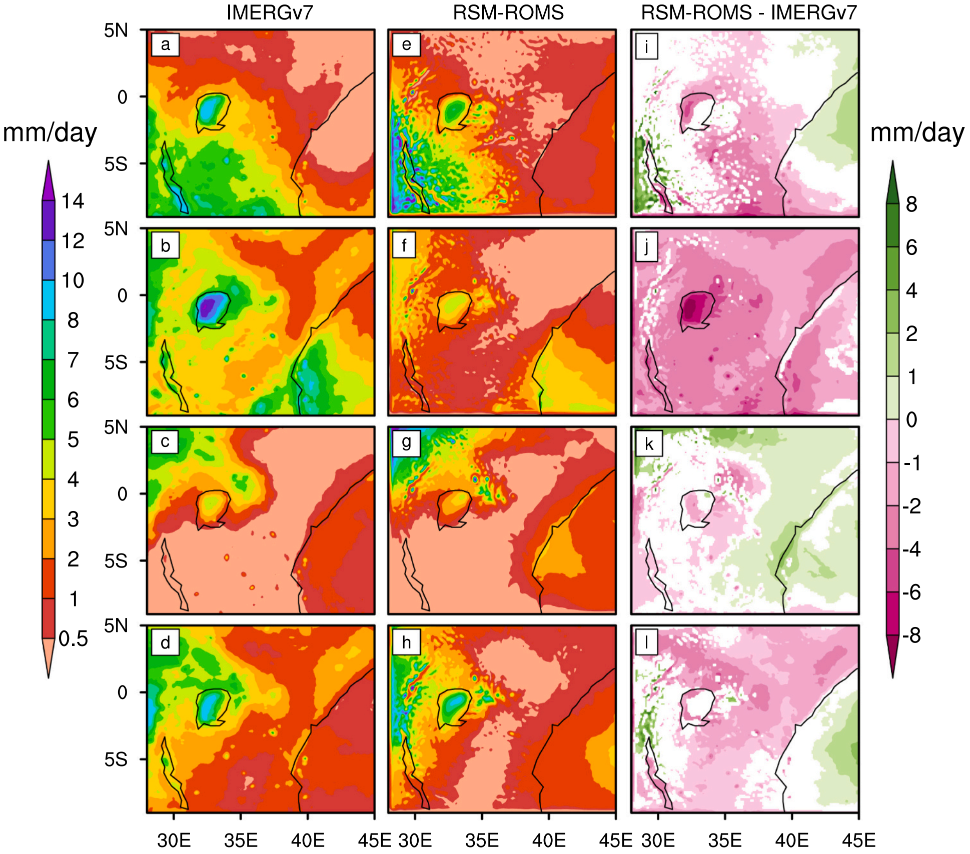

Fig. 2. The seasonal mean climatological precipitation (mm/day) from (a, b, c, d) IMERG and (e, f, g, h) RSM-ROMS for (a, e) DJF, (b, f) MAM, (c, g) JJA, and (d, h) SON seasons. The corresponding systematic errors of seasonal mean precipitation (mm/day) from RSM-ROMS for (i) DJF, (j) MAM, (k) JJA, and (l) SON seasons. Only statistically significant differences at 95 % confidence interval according to *t*-test are shaded in panels i, j, k and l.

the i^{th} harmonic (with $i = 1$ corresponding to diurnal harmonic), and $\theta = \frac{2\pi t_k}{N}$, $t_k = \{00, 01, 02, 03, \ldots .24\}$, respectively. The intraseasonal variance of daily precipitation is computed using the first order, recursive, bandpass (20–50 days) Butterworth Filter (Butterworth, 1930). In these filters the filtered value depends not only on a weighted averaged of the unfiltered time series but also recursively on previous values in the filtered time series. One advantage of these techniques is their ability to achieve rapid convergence compared to conventional filters that rely on weighted averages. Additionally, these techniques allow for the specification of the peak in the response curve at any desired bandwidth (Krishnamurti et al., 1990).

5. Results

i) Seasonal Climatology

a) Rainfall

In Fig. 2a-d we show the observed seasonal mean climatology of the rainfall for DJF, MAM, JJA and SON, respectively. The corresponding objective scores of pattern correlations and standardized variance of tie simulated climatological precipitation are shown in the Taylor Diagram in the supplementary material (Fig. S1). The complex seasonal cycle with the annual peak of rainfall in DJF over

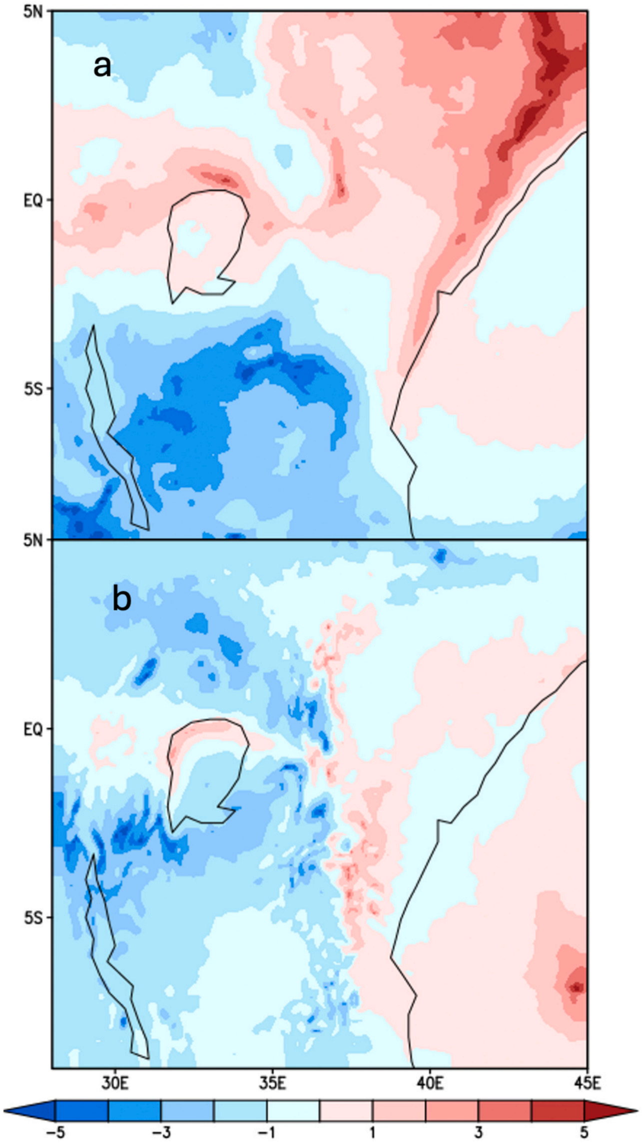

Fig. 3. The distribution of the rainfall given by $\log_2\left|\frac{a_2}{a_1}\right|$, where a_1 and a_2 are the Fourier harmonics of the annual and semi-annual period, respectively from (a) IMERG and (b) RSM-ROMS. The positive and negative values suggest the semiannual and annual components of rainfall are dominant, respectively.

southern Tanzania and the semi-annual cycle of rainfall over Kenya and Somalia is apparent from these figures. The corresponding seasonal climatology from RSM-ROMS is shown in Fig. 2e-h, which shows similar spatial heterogeneity in the seasonal cycle of rainfall across the domain. The systematic errors however indicate that the errors of the RSM-ROMS simulation are maximum in the MAM season (Fig. 2j) and comparatively far less in the rest of the year. In the MAM season, the dry bias is spread across the domain, dominated by the most severe dry bias over Lake Victoria. The seasonal precipitation bias is the least in the DJF season (Fig. 2i). However, it is well known that Lake Victoria has a large annual mean rainfall of over 1800 mm (Yin and Nicholson, 1998; Yin et al., 2000), which is partly a result of the mesoscale low feature that develops over the lake (Nicholson, 2017). The Taylor Diagram in Fig. S1 suggests that the variance of precipitation in RSM-ROMS is comparable to observations in DJF (Fig. S1a) and SON (Fig. S1d) while it is underestimated and overestimated in MAM (Fig. S1b) and JJA (Fig. S1c) seasons, respectively. The pattern correlation is above 0.7 in all seasons (Fig. S1).

To further examine the spatial distribution of the annual rainfall types in the region, we show in Fig. 3 the ratio of $\left|\frac{a_2}{a_1}\right|$, where a_2 is the amplitude of semi-annual period harmonic and a_1 is the annual period harmonic from observations and the RSM-ROMS simulation. The observations in Fig. 3a show that in the northeast and central parts of the domain, which include parts of Somalia, Kenya, southern Uganda, and eastern DRC are dominated by the semiannual component of rainfall. In contrast, Tanzania towards the south of the domain and northern Uganda, South Sudan in the north of the domain is dominated by the unimodal distribution of the seasonal cycle (Fig. 3a). This distribution of rainfall is largely observed in the RSM-ROMS simulation (Fig. 3b), although the dominance of the semiannual component of rainfall is underestimated over eastern Kenya, Somalia, southern Uganda, and eastern DRC. Similarly, the dominance of the annual harmonic over Tanzania is underestimated in the RSM-ROMS simulation (Fig. 3b). Over the oceans, the semi-annual component of rainfall is dominant only around 5°S in the observations (Fig. 3a) while in the RSM-ROMS simulation, it is dominant across the western Indian Ocean included in the domain (Fig. 3b).

b) Precipitable water

The humidity content in the atmospheric column plays an important role in the modulation of precipitation in the tropics

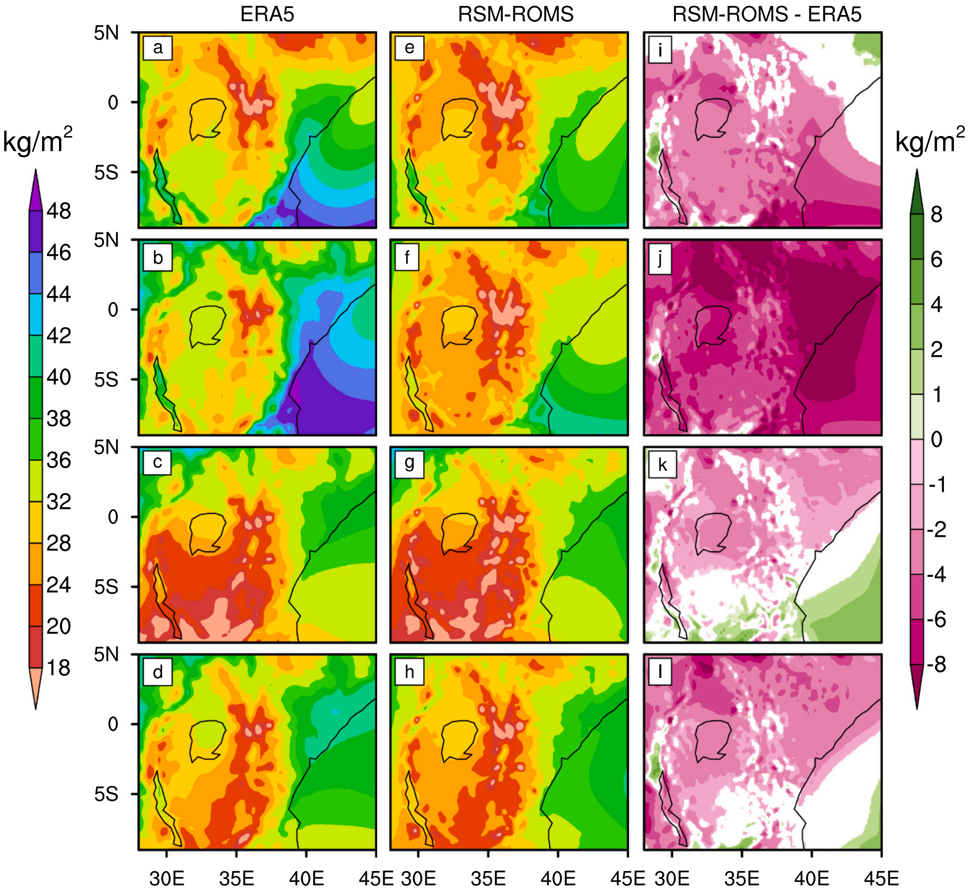

Fig. 4. The seasonal mean climatological precipitable water (kg/m^2) from (a, b, c, d) ERA5 and (e, f, g, h) RSM-ROMS for (a, e) DJF, (b, f) MAM, (c, g) JJA, and (d, h) SON seasons. The corresponding systematic errors of seasonal mean precipitable water (kg/m^2) from RSM-ROMS for (i) DJF, (j) MAM, (k) JJA, and (l) SON seasons. Only statistically significant differences at 95 % confidence interval according to *t*-test are shaded in panels i, j, k and l.

(Raymond, 2000; Bretherton et al., 2004). This connection is through the tight coupling in the tropics between the precipitable water and the moist static energy in the atmospheric column owing to the weak temperature gradient in the tropics (Yasunaga and Mapes, 2012), which in turn is strongly related to the corresponding precipitation anomalies. In Fig. 4 we show the comparison of the seasonal cycle of precipitable water from ERA5 and RSM-ROMS simulation. The precipitable water in ERA5 is largest over oceans and adjacent coastal regions of Tanzania, Kenya, and Somalia in DJF and MAM seasons. The spatial heterogeneity in the dominance of annual and semi-annual cycle is also apparent in the precipitable water with the latter dominant in coastal Kenya and Somalia and the former over Tanzania, South Sudan, and northern Uganda (Fig. 4a-d). This is in large part also apparent in the RSM-ROMS simulation (Fig. 4e-h), although the precipitable water is underestimated across the domain (Fig. 4i-l). The largest dry bias appears in the MAM season (Fig. 4j) while it is the least in the JJA season (Fig. 4k). This dry bias in the precipitable water across the year in the RSM-ROMS simulation is consistent with the dry precipitation bias alluded earlier (Fig. 2i-l). The pattern correlation of RSM-ROMS simulation with the ERA5 reanalysis is above 0.9 in all seasons (Fig. S1) while the corresponding variance is underestimated in DJF (Fig. S1a) and MAM (Fig. S1b) and is comparable in JJA (Fig. S1c) and SON (Fig. S1d) seasons.

c) Sea Surface Temperature (SST)

The SST is a prognostic variable in RSM-ROMS since it is a coupled ocean-atmosphere model. The seasonal cycle of the observed SST (Fig. 5a-d) indicates that the annual peak is in DJF (Fig. 5a) while the annual nadir is in JJA (Fig. 5c) season in the tropical western Indian Ocean. We see a similar seasonal cycle in the RSM-ROMS simulation (Fig. 5e-h). However, the annual peak of SST in DJF (Fig. 5e) in the RSM-ROMS is not distinct from the MAM (Fig. 5g) season. The systematic errors of the simulation in Fig. 5i-l suggests that the seasonal errors are statistically significant in the DJF season only with a cold bias of ≤ -1℃. In the rest of the year the simulation shows a statistically insignificant difference from the corresponding observations (Fig. 5j-l). The lake temperatures in the RSM-ROMS simulation are comparatively higher with temperatures $> 29^\circ$C compared to other high-resolution modeling studies of the lake which suggest an annual mean surface temperature of around 25°C to 27°C (Sun et al. 2015; Nyamweya et al. 2016; Van de Walle et al., 2020). The lake temperatures also display a seasonal cycle albeit weakly with Lake Tanganyika showing a peak in the boreal spring season while Lake Victoria shows an annual peak in the JJA season (Fig. 5e-h), which is consistent for the latter with other prior studies (Sun et al. 2015; Naymweya et al., 2016). The pattern correlations for the SST from the RSM-ROMS simulation with the

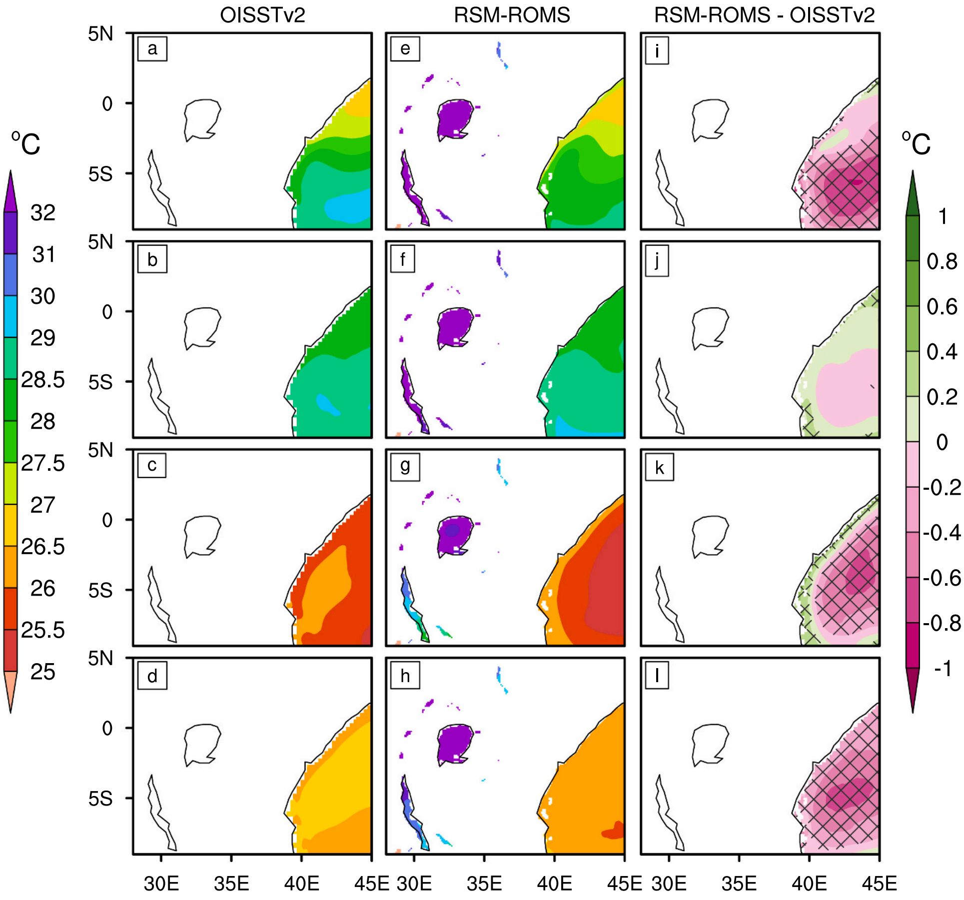

Fig. 5. The seasonal mean SST (°C) from (a, b, c, d) OISST and (e, f, g, h) RSM-ROMS for (a, e) DJF, (b, f) MAM, (c, g) JJA, and (d, h) SON seasons. The corresponding systematic errors of seasonal mean SST (°C) from RSM-ROMS for (i) DJF, (j) MAM, (k) JJA, and (l) SON seasons. The statistically significant differences at 95 % confidence interval according to *t*-test are hatched in panels i, j, k and l.

corresponding observations is 0.91, 0.86, 0.39, and 0.52 for DJF, MAM, JJA, and SON seasons, respectively.

d) Ocean mixed layer

The mixed layer depth in the western Indian Ocean undergoes significant seasonality owing primarily to the reversal of the winds from the northeast to southwesterly monsoon winds from boreal winter to summer. Therefore, the mixed layer depth is extremely shallow in DJF (Fig. 6a) when downwelling circulations are dominant and deepest in JJA (Fig. 6c) seasons when the upwelling circulations are strongest, which lead to a strong modulation of the upper ocean stratification. The RSM-ROMS show a similar seasonal cycle as the observations (Fig. 6e-h). The mixed layer depth is diagnosed from the density profile following Monteguet et al., 2004. Therefore, the mixed layer depth is defined as the depth at which density is equal to surface density plus the density difference brought about by temperature increment of 0.2 °C. The strongest seasonal cycle is displayed along the coast and there is a clear underestimation of the mixed layer depth all-round the year with JJA showing the largest bias (Fig. 6i-l). The mixed layer depth in the lakes also shows a seasonal cycle with the largest depths in the boreal summer (Fig. 6e-h). The pattern correlations for the mixed layer depth from the RSM-ROMS simulation with the corresponding observations is 0.56, 0.27, 0.51, and −0.13 for DJF, MAM, JJA, and SON seasons, respectively. The negative pattern correlations in the SON season suggests the poor simulation of the mixed layer depth spatial gradients as is apparent from comparing Fig. 6d and h.

e) Thermocline depth

The thermocline depth often diagnosed from the depth of the 20°C isotherm marks the boundary between the fresh and warm upper ocean from the cold and saline deep ocean. Unlike the SST and the mixed layer depth, the seasonal cycle of the thermocline depth is much weaker (Fig. 7a-d). The average depth of the thermocline is over 90 m across the year (Fig. 7a-d), which is clearly underestimated in the RSM-ROMS simulation (Figs. 7e-h and 7i-l). Therefore, in terms of the ocean stratification, it may be concluded from Figs. 6 and 7 that the RSM-ROMS simulation of this study is more strongly stratified in a shallower depth than the corresponding observations. This could be a result of insufficient mixing in the upper ocean or bias in the forcing to the ocean, which is always difficult to separate in a coupled framework like the RSM-ROMS. The pattern correlations for the depth of the 20°C isotherm from the RSM-ROMS simulation with the corresponding observations is 0.69, 0.66, 0.81, 0.69 for DJF, MAM, JJA, and SON seasons, respectively.

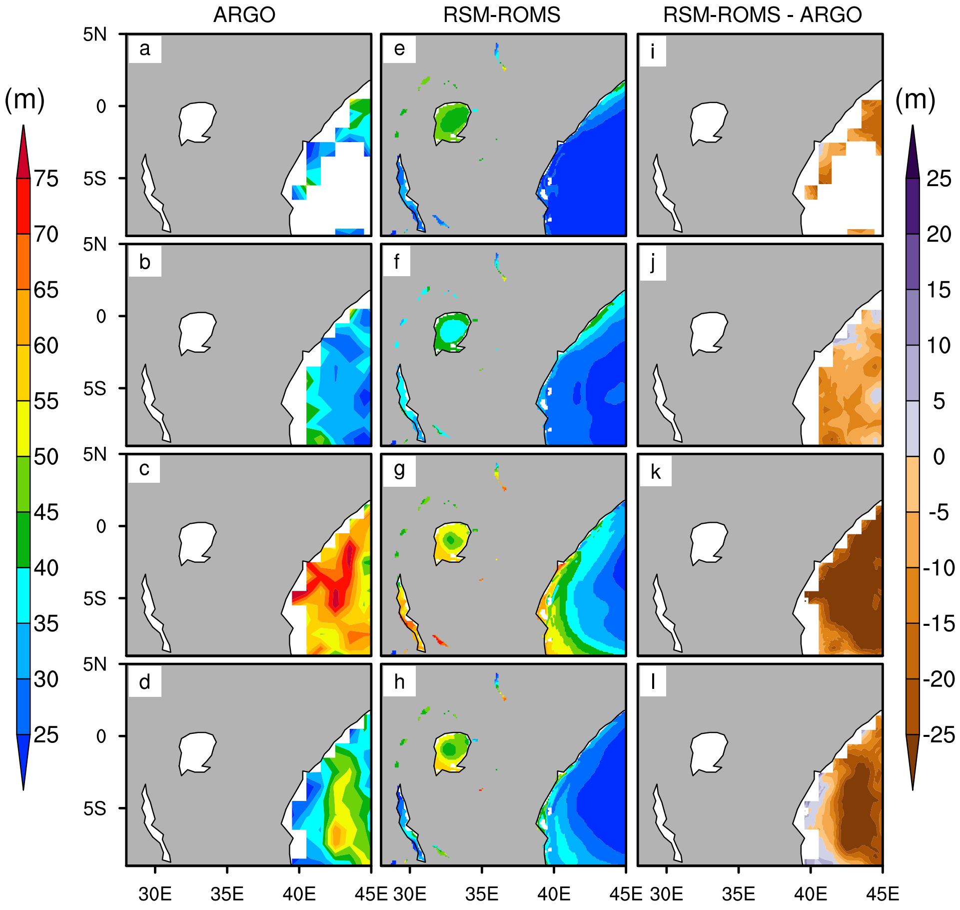

Fig. 6. The seasonal mean mixed layer depth (m) from (a, b, c, d) ARGO and (e, f, g, h) RSM-ROMS for (a, e) DJF, (b, f) MAM, (c, g) JJA, and (d, h) SON seasons. The corresponding systematic errors of seasonal mean mixed layer depth (m) from RSM-ROMS for (i) DJF, (j) MAM, (k) JJA, and (l) SON seasons. Only statistically significant differences at 95 % confidence interval according to *t*-test are shaded in panels i, j, k and l.

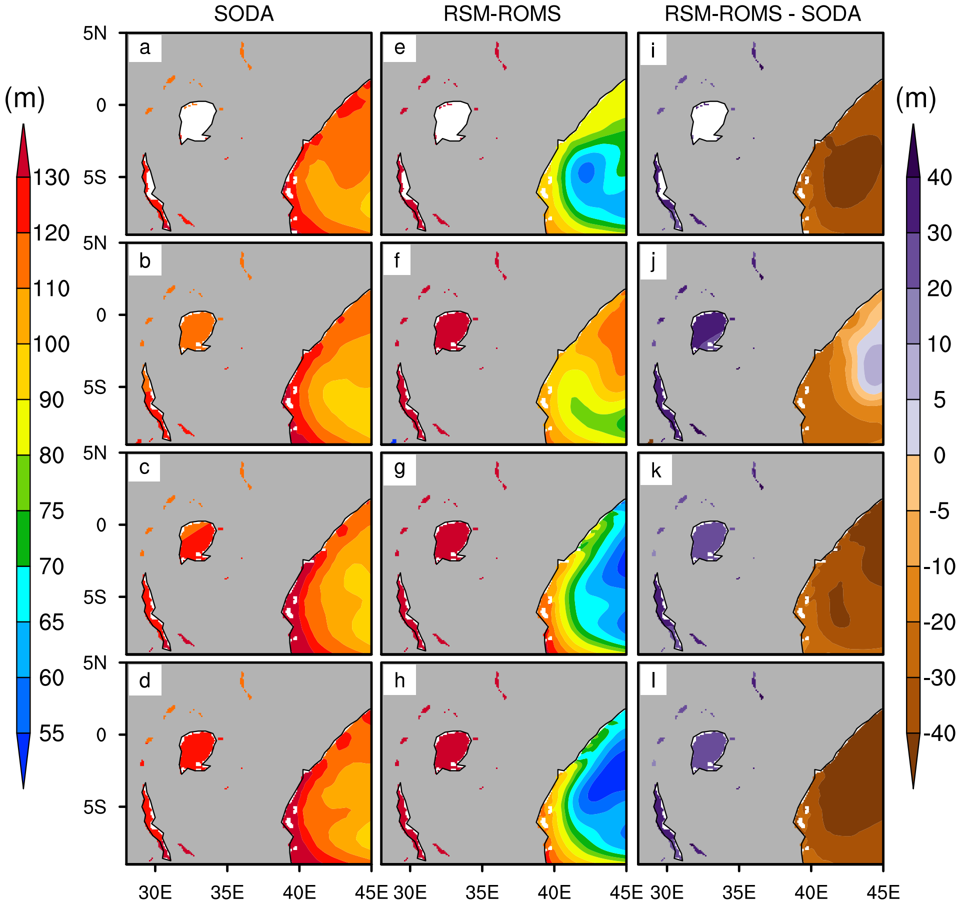

Fig. 7. The seasonal mean depth of the 20°C isotherm (m) from (a, b, c, d) SODA and (e, f, g, h) RSM-ROMS for (a, e) DJF, (b, f) MAM, (c, g) JJA, and (d, h) SON seasons. The corresponding systematic errors of seasonal mean depth of the 20°C (m) from RSM-ROMS for (i) DJF, (j) MAM, (k) JJA, and (l) SON seasons. Only statistically significant differences at 95 % confidence interval according to *t*-test are shaded in panels i, j, k and l.

f) Winds

In an annual mean sense the low-level tropospheric flow over the GHA is dominated by southerlies which becomes southwesterlies as they cross the equator (Paegle and Geisler, 1986; Slingo et al., 2005; Nicholson, 2017). This is also observed in Fig. 8 (showing the 850 hPa winds) where the southerlies are dominating in 3 of the 4 seasons of the year. The DJF season shows the northerly flow with the northeasterly flow north of 2°S in both ERA5 and RSM-ROMS simulation. Turkana Jet is a well-known mesoscale feature of the region which passes through the Turkana Channel between the Ethiopian and East African Highlands (Kinuthia and Asnani, 1982; Kinuthia, 1992). It essentially exists throughout the year because of the orographic channeling of the winds (Sun et al., 1999). The jet exhibits a strong diurnal variation with a nocturnal maximum resulting from the orographic downslope winds strengthened by the drier conditions in the Turkana Channel and surrounding mountains from the comparatively strong windspeeds of the jet (Vizy and Cook 2019). The persistence of this jet throughout the year is seen in both ERA5 and in the RSM-ROMS simulation. Furthermore, the seasonal variations of the jet in RSM-ROMS are comparable with ERA5. The pattern correlations of the zonal and meridional winds and wind speeds at 850hPa from RSM-ROMS with ERA5 reanalysis is above 0.6 across the year and the variances are also nearly comparable (Fig. S1). However, the variance of the 850hPa meridional wind is slightly underestimated more than the zonal wind except in the SON season (Fig. S1).

At 200hPa the flow is dominated by easterlies for most of the year except in the SON season when the westerlies appear south of the equator and the easterlies are extremely weak north of the equator (Fig. 9a-d). The seasonal cycle of the 200hPa winds is reasonable in RSM-ROMS simulation in comparison to ERA5. The most widespread bias in the RSM-ROMS simulation is in the DJF season (Fig. 9i) while in the rest of the year the easterlies are stronger than ERA5 in the western part of the domain. The pattern correlations of the zonal and meridional winds and wind speeds at 200 hPa from RSM-ROMS with ERA5 reanalysis is above 0.6 in DJF (Fig. S1a) and JJA (Fig. S1c) seasons. But in MAM season the pattern correlation of meridional wind is less than 0.1 while that of zonal wind is 0.9 (Fig. S1b). Although the variance of the zonal wind is slightly overestimated, that of the meridional wind and wind speed is significantly overestimated in MAM in the RSM-ROMS simulation (Fig. S1b). The meridional wind continues to show poor skills in the SON season (Fig. S1d).

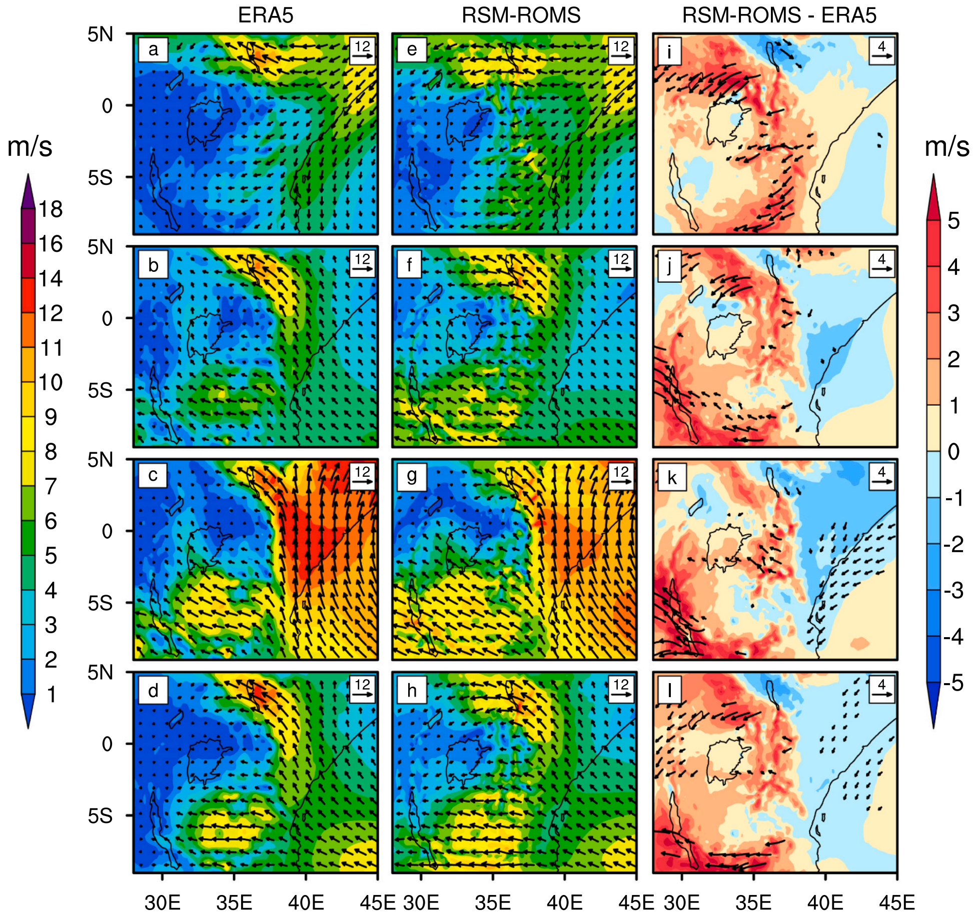

Fig. 8. The seasonal mean winds at 850 hPa (m/s) from (a, b, c, d) ERA5 and (e, f, g, h) RSM-ROMS for (a, e) DJF, (b, f) MAM, (c, g) JJA, and (d, h) SON seasons. The corresponding systematic errors of 850 hPa winds (m) from RSM-ROMS for (i) DJF, (j) MAM, (k) JJA, and (l) SON seasons. In panels i, j, k, and l, vectors are shown for statistically significant differences at 95 % confidence interval according to *t*-test.

ii) Diurnal variability

We isolate the diurnal variations by isolating the local diurnal harmonic following Dai and Wang (1999). The largest diurnal amplitudes are found over Lake Victoria and around it in boreal spring and fall seasons (Fig. 10). The late evening-early morning diurnal maximum over Lake Victoria was noted in several other studies (Yin and Nicholson, 1998; Yin et al., 2000; Camberlin et al., 2017, 2019) is also observed both in IMERG as well as in the RSM-ROMS simulation across all seasons in Fig. 10a-d with the diurnal peak of rainfall occurring between 0000 and 0600 LST. The seasonality of the diurnal variations over Lake Victoria, Lake Tanganyika, and the surrounding land regions is also distinct with the MAM (long rains) season displaying an annual peak in the diurnal amplitude followed by the next maximum in the short rains season of SON.

The climatological seasonal average diurnal variations of rainfall from IMERG and RSM-ROMS simulation is shown in Fig. 10 as vector plots with the length and direction indicating the magnitude and timing of the diurnal maximum of rainfall (in local solar time), respectively. The diurnal amplitude over the land regions south and east of Lake Victoria is comparatively weaker than north and west of the lake in IMERG and RSM-ROMS (Fig. 10a-d). The seasonal variability of the diurnal cycle of precipitation closely follows the annual cycle of precipitation shown in Fig. 2 with the drier part of the year of JJA having the weakest diurnal signal and long rain season of MAM having the strongest diurnal signal. The diurnal cycle of rainfall over Lake Victoria is persistent throughout the year with comparable magnitude and a slight shift in the timing of the diurnal peak from one season to the next in the observations. RSM-ROMS shows similar persistence in amplitude and timing of the diurnal peak across the year over Lake Victoria. The seasonality of the diurnal variations of the rainfall is far stronger in the terrestrial regions around Lake Victoria, especially over Uganda and western Kenya, which coincides with the seasonal cycle of rainfall shown earlier in Fig. 2. This seasonality of the diurnal cycle is most prominent over Lake Victoria which has the most annual rainfall in the domain (Fig. 2). These are regions where the model simulations show some of the largest discrepancy in the timing of the diurnal peak of rainfall besides near the western edge of the domain. The land regions east of Lake Victoria that display a late afternoon diurnal maximum are modulated by the large-scale easterlies and topography (Van de Walle et al., 2020).

The RSM-ROMS simulation has a systematic bias of underestimating the amplitude of the diurnal cycle of rainfall relative to IMERG

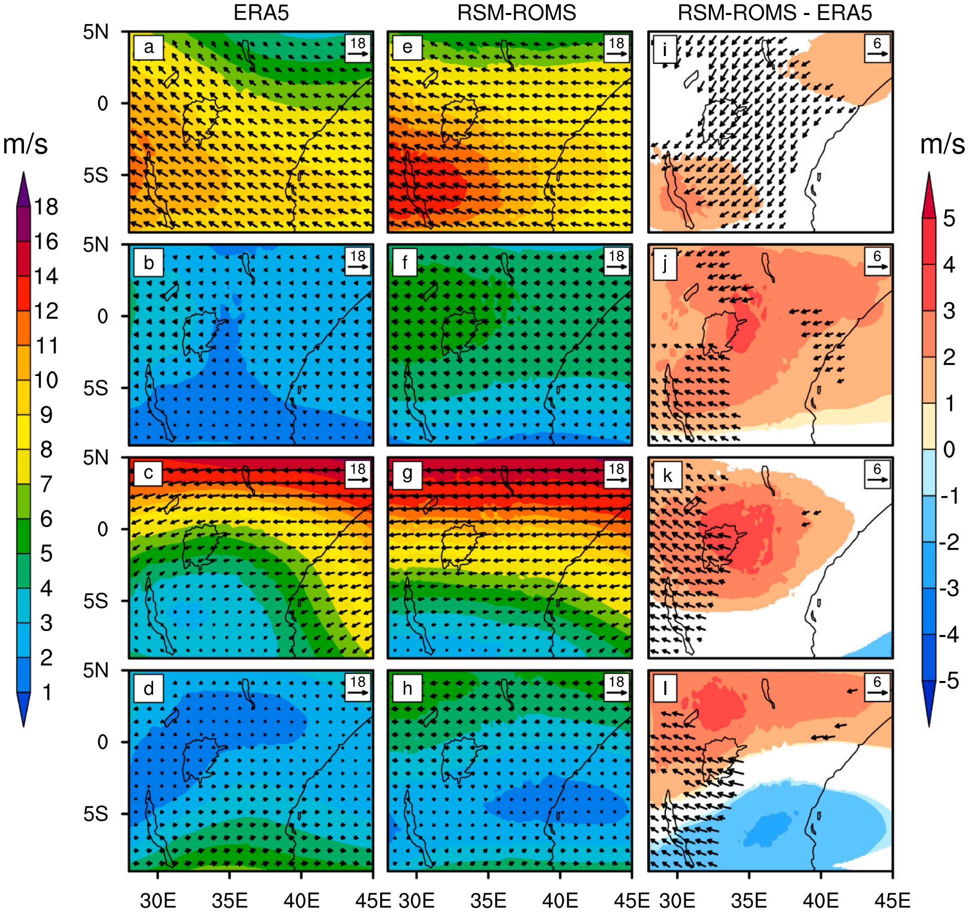

Fig. 9. The seasonal mean winds at 200 hPa (m/s) from (a, b, c, d) ERA5 and (e, f, g, h) RSM-ROMS for (a, e) DJF, (b, f) MAM, (c, g) JJA, and (d, h) SON seasons. The corresponding systematic errors of 200 hPa winds (m) from RSM-ROMS for (i) DJF, (j) MAM, (k) JJA, and (l) SON seasons. In panels i, j, k, and l, vectors are shown for statistically significant differences at 95 % confidence interval according to *t*-test.

across the domain in all four seasons (Fig. 10). Furthermore, there are some relatively large differences in the phase, especially over Lake Victoria and northeast of it ranging anywhere from an hour (Fig. 10a) to over 4 hours (Fig. 10b-d). Nonetheless, the spatial gradients in the timing and the amplitude of the diurnal maximum of precipitation are captured by RSM-ROMS over and around the lake, which reasonably verifies with IMERG.

iii) Intraseasonal variability

The intraseasonal variance of daily precipitation is computed using the first order, recursive, bandpass (20–50 days) Butterworth Filter (Butterworth, 1930). Fig. 11 shows the 20–50 days band passed variance of precipitation during the October-December season when the intraseasonal variations are most active in the region (Camberlin et al. 2019). The large intraseasonal variance over Lake Victoria and Lake Tanganyika in the observations (Fig. 11a) are captured in the RSM-ROMS simulation (Fig. 11b). However, besides this verification, the pattern of 20–50 days variance between the simulation and observations is quite different. For instance, the model simulation has a comparatively much weaker variance along the eastern terrestrial corridor from Tanzania to Somalia. This region of weak intra-seasonal variance in RSM-ROMS is in between regions of high intraseasonal variance along the eastern boundary over the western Indian Ocean and the western boundary along the DRC (Fig. 11b), which is unsupported by observations (Fig. 11b). This bias in the variance of the 20–50 days intraseasonal variations is like the seasonal mean precipitation bias for the boreal fall and winter seasons in Fig. 2i and l, respectively. In other words, the dry seasonal bias along the eastern terrestrial corridor from Tanzania to Somalia and the wet bias over the western Indian Ocean could be influencing the corresponding reduction and increase in intra-seasonal variations, respectively.

6. Conclusions

In this study we have conducted a thorough analysis of the fidelity of a 25-year simulation from a regional coupled ocean-atmosphere model (RSM-ROMS) over eastern equatorial Africa which included parts of the GHA. This is first of its kind regional climate model with the inclusion of the coupled air-sea interactions at 10 km grid resolution over GHA. The model shows reasonable

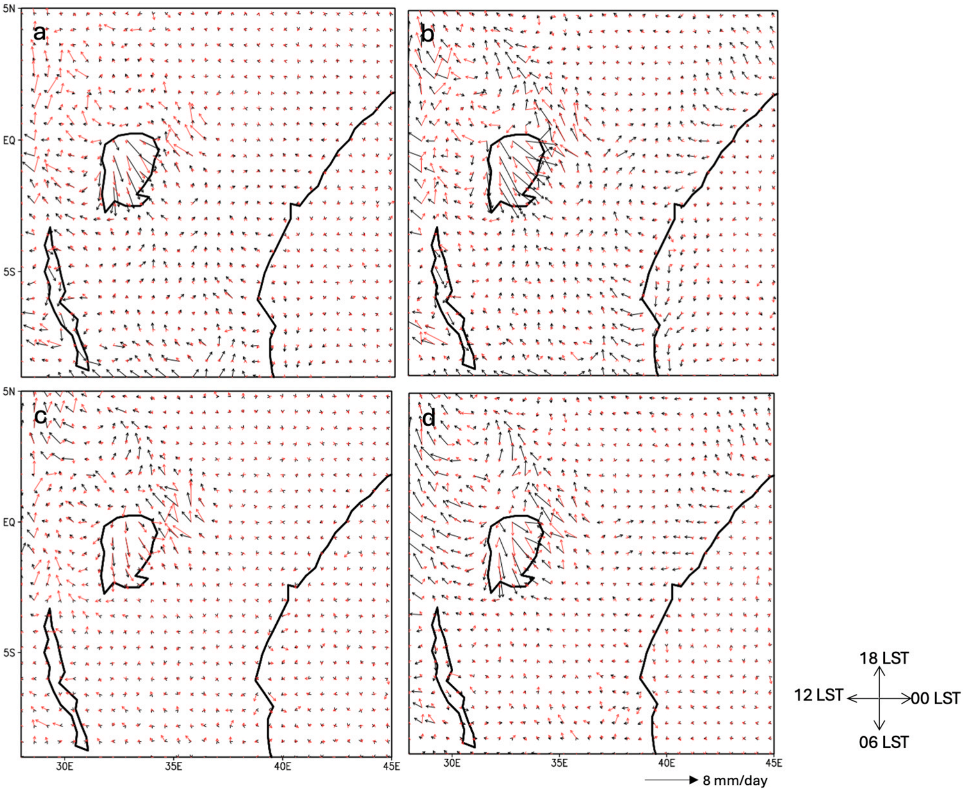

Fig. 10. The climatological diurnal amplitude (mm/day) and phase (LST) of rainfall from IMERG (black vector) and RSM-ROMS (red vector) for a) DJF, b) MAM, c) JJA, and d) SON seasons.

fidelity with regard to the seasonal cycle of rainfall, precipitable water, lower and upper tropospheric winds, SST, mixed layer depth, and the depth of the thermocline. However, the systematic dry precipitation and precipitable water bias, the stronger than observed upper ocean stratification with shallower mixed layer and thermocline depth are concerning factors of the simulation. The highlight of the simulation is that RSM-ROMS is able to show the spatial distribution of the bimodal and unimodal peaks of the seasonal cycle of rainfall that verify well with the observations. Another highlight of the simulation is its reasonable verification of the diurnal variation of the rainfall. The largest amplitude of this variation appearing over Lake Victoria and the timing of this maximum shifting from local early morning over the lake to afternoon along the east coast of GHA and late afternoon elsewhere around the lake are verified features of the simulation. The diurnal variations over Lake Victoria are persistent across all seasons, although they amplify during the long and short rainy seasons. The terrestrial regions around Lake Victoria show a larger seasonal variability in the diurnal cycle of rainfall, especially over western Kenya and Uganda. Nonetheless, the bias of lower magnitude of the diurnal variations and the timing of diurnal peaks are largest in these regions (except near the western boundary of the domain) in the RSM-ROMS simulation is apparent.

Similarly, the intraseasonal variance of the precipitation in the October-December season shows a maximum over the Lake both in the observations and in the RSM-ROMS simulation. However, the sub-seasonal or intraseasonal variance in the simulation is underestimated over coastal areas of GHA and inland over Somalia, Kenya, and Tanzania, while it is overestimated along the western boundary of the domain (over DRC) and in the east over the western Indian Ocean.

Admittedly, a single integration for the 25-year period from a coupled model like RSM-ROMS is insufficient to assess the model for interannual and longer-term variations. However, the mean bias and variations at shorter diurnal and intraseasonal scales can be assessed robustly from this 25 year integration. Furthermore, the advantage of air-sea coupling in RSM-ROMS is not abundantly clear from this study. But in our future work when we deploy this model for climate change projections for the region, it will become apparent that integrating a coupled ocean-atmosphere model like RSM-ROMS would be a natural choice to allow the local air-sea coupling to evolve future state of the regional terrestrial and ocean climate.

CRediT authorship contribution statement

C. B. Jayasankar: Writing – review & editing, Visualization, Validation, Methodology, Data curation. **Vasubandhu Misra:** Writing – review & editing, Writing – original draft, Visualization, Validation, Methodology, Funding acquisition, Conceptualization.

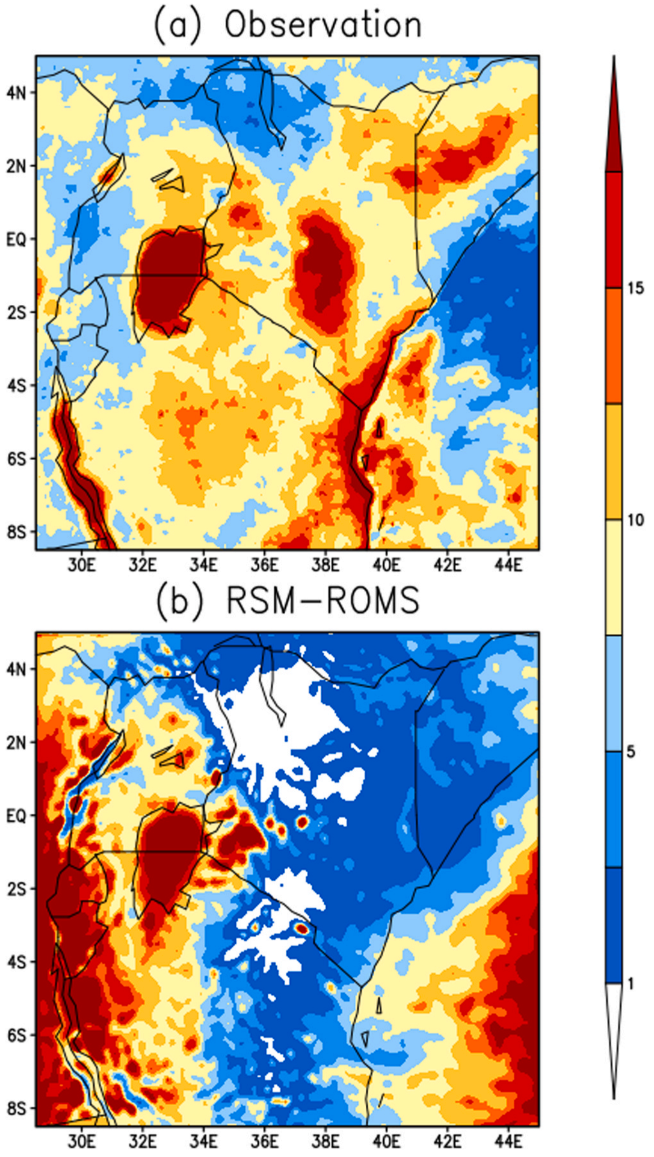

Fig. 11. The intraseasonal (20–50 days) variance of precipitation ($\left[\frac{mm}{day}\right]^2$) from a) observations and b) RSM-ROMS averaged for the October-November-December season.

Declaration of Competing Interest

The authors declare the following financial interests/personal relationships which may be considered as potential competing interests: Vasubandhu Misra reports financial support was provided by NASA Goddard Space Flight Center. If there are other authors, they declare that they have no known competing financial interests or personal relationships that could have appeared to influence the work reported in this paper.

Acknowledgements

We acknowledge the support from NASA grant 80NSSC22K0595. The IMERG dataset was provided by the NASA/Goddard Space Flight Center and PPS which developed and computed the IMERG as a contribution to GPM and archived at the NASA GES DISC.

Appendix A. Supporting information

Supplementary data associated with this article can be found in the online version at doi:10.1016/j.dynatmoce.2024.101520.

Data availability

The IMERG rainfall from NASA was obtained from (IMERG, 2022). The ERA5 reanalysis data was from (ERA5, 2022), the mixed layer depth from Argo was obtained from (Holte et al., 2017) and the SODA v2.2.4 ocean reanalysis data was obtained from SODA (2022). The NCEP-DOE (R2) reanalysis data at 6 hourly interval was obtained from UCAR (2022) or alternatively the data can also be accessed from PSL (2022). The data from the RSM-ROMS integration to generate the figures in the manuscript will be made available upon request.

References

Alpert, J.C., Kanamitsu, M., Caplan, P.M., Sela, J.G., White, G., Kalnay, E., 1988. Mountain induced gravity wave drag parameterization in the NMC medium-range forecast model. In: Proceedings of the Eighth Conf. on Numerical Weather Prediction. Amer. Meteor. Soc, Baltimore, MD, pp. 726–733.

Bahaga, T.K., Mengistu Tsidu, G., Kucharski, F., Diro, G.T., 2015. Poten- tial predictability of the sea-surface temperature forced equato- rial East African short rains interannual variability in the 20th century. Q J. R. Meteor. Soc. 141 (686), 16–26 https://doi. org/10.1002/qj.2338.

Black, E., Slingo, J., Sperber, K.R., 2003. An observational study of the relationship between excessively strong short rains in coastal East Africa and Indian Ocean SST. Mon.

Bretherton, C.S., Peters, M.E., Back, L.E., 2004. Relationships between water vapor path and precipitation over the tropical oceans. J. Clim. 17, 1517–1528.

Bryson, R.A., Kuhn, P.M., 1961. Stress-differential induced-divergencewith applicationto littoral precipitation. Erdkunde 15, 287–294.

Butterworth, S., 1930. On the theory of filter amplifiers. Wirel. Eng. 7, 536–541 (q!:q!).

Camberlin, P., Gitau, W., Kiladis, G., Bosire, E., Pohl, B., 2019. Intraseasonal to interannual modulation of diurnal precipitation distribution over Eastern Africa. J. Geophys. Res. Atmos. 124 (11), 863–886. https://doi.org/10.1029/2019JD031167.

Camberlin, P., Gitau, W., Planchon, O., Dubreuil, V., Funatsu, B.M., Philippon, N., 2017. Major role of water bodies on diurnal precipitation regimes in Eastern Africa. Int. J. Climatol. 38 (2), 613–629. https://doi.org/10.1002/joc.5197.

Camberlin, P., Wairoto, J., 1997. Intraseasonal wind anomalies related to wet and dry spells during the “long” and “short” rainy seasons in Kenya. Theor. Appl. Climatol. 58 (1–2), 57–69. https://doi.org/10.1007/BF00867432.

Carton, J.A., Giese, B.S., 2008. A reanalysis of ocean climate using Simple Ocean Data Assimilation (SODA). Mon. Weather Rev. 136, 2999–3017. https://doi.org/10.1175/2007MWR1978.1.

Chou, M.D., Lee, K.T., Tsay, S.C., Fu, Q., 1999. Parameterization for cloud longwave scattering for use in atmospheric models. J. Clim. 12 (1), 159–169.

Chou, M.D., Lee, K.T., 1996. Parameterizations for the absorption of solar radiation by water vapor and ozone. J. Atmos. Sci. 53, 1203–1208.

Cook, K.H., Vizy, E.K., 2013. Projected changes in EA rainy seasons. J. Clim. 26 (16), 5931–5948. https://doi.org/10.1175/JCLI-. D-12-00455.1.

Dai, A., Wang, J., 1999. Diurnal and semidiurnal tides in global surface pressure fields. J. Atmos. Sci. 56, 3874–3891.

Danielson, J.J., Gesch, D.B., 2011. Global multi-resolution terrain elevation data. Report Number: Open-File Report 2011–1073. https://doi.org/10.3133/ofr20111073.

Dunning, C.M., Allan, R.P., Black, E., 2017. Identification of deficiencies in seasonal rainfall simulated by CMIP5 climate models. Environ. Res. Lett. 12, 114001 (Art. No).

Ek, M.B., Mitchell, K.E., Lin, Y., Rogers, E., Grunmann, P., Koren, V., Gayno, G., Tarpley, J.D., 2003. Implementation of Noah land surface model advances in the National Centers for Environmental Prediction operational mesoscale Eta model. J. Geophys. Res. 108, 8851. https://doi.org/10.1029/2002JD003296.

Endris, H.S., Omondi, P., et al., 2013. Assessment of the performance of CORDEX regional climate models in simulating East African rainfall. J. Clim. 26 (21), 8453–8475. https://doi.org/10.1175/JCLI-. D-12-00708.1.

ERA5, 2022: ⟨https://www.ecmwf.int/en/forecasts/datasets/reanalysis-datasets/era5⟩.

Ezer, T., Arango, H., Shchepetkin, A.F., 2002. Developments in terrain-following ocean models: intercomparisons of numerical aspects. Ocean Model. 4, 249–267.

Funk, C., et al., 2018. Examining the role of unusually warm Indo-Pacific sea-surface temperatures in recent African droughts. Q. J. R. Meteorol. Soc. 144, 3266.

Haidvogel, D.B., Arango, H.G., Hedstrom, K., Beckmann, A., Malanotte-Rizzoli, P., Shchepetkin, A.F., 2000. Model evaluation experiments in the North Atlantic Basin: simulations in nonlinear terrain-following coordinates. Dyn. Atmos. Oceans 32 (3), 239–281.

Ham, S., Yoshimura, K., Li, H., 2016. Historical dynamical downscaling for East Asia with the atmosphere and ocean coupled regional model. J. Meteorol. Soc. Jpn. 94A, 199–208. https://doi.org/10.2151/jmsj.2015-046.

Han, F., Cook, K.H., Vizy, E.K., 2019. Changes in intense rainfall events and dry periods across Africa in the twenty-first century. Clim. Dyn. https://doi.org/10.1007/s00382-019-04653-z.

Hastenrath, S., Nicklis, A., Greischar, L., 1993. Atmospheric-hydrospheric mechanisms of climate anomalies in the western equatorial Indian Ocean. J. Geophys. Res. Oceans 98 (C11), 20219–20235. https://doi.org/10.1029/93JC02330.

Hastenrath, S., Polzin, D., Mutai, C., 2011. Circulation mechanisms of Kenya rainfall anomalies. J. Clim. 24 (2), 404–412. https://doi.org/10.1175/2010JCLI3599.

Herrmann, S.M., Mohr, K.I., 2011. A continental-scale classifi- cation of rainfall seasonality regimes in Africa based on gridded precipitation and land surface temperature products. J. Appl. Meteor. 50 (12), 2504–2513. https://doi.org/10.1175/JAMC-D-11-024.1.

Hersbach, H., Bell, W., Berrisford, P., Horanyi, A., Sabater, J.M., Nicolas, J., Peubey, C., Radu, R., Schepers, D., Simmons, A., Soci, C., Abdalla, S., Abellan, X., Balsamo, G., Bechtold, P., Biavati, G., Bidlot, J., Nonavita, M., De Chiara, G., Dahlgren, P., Dee, D., Diamantakis, M., Dragani, R., Flemming, J., Forbes, R., Fuentes, M., Geer, A., Jaimberger, L., Healy, S., Hogan, R.J., Holm, E., Janiskova, M., Keeley, S., Laloyaux, P., Lopez, P., Lupu, C., Radnoti, G., de Rosnay, P., Rozum, I., Vamborg, F., Villaume, S., Thepaut, J.-N., 2019. The ERA5 global reanalysis. Q. R. Met. Soc. https://doi.org/10.1002/qj.3803.

Holte, J., Talley, L.D., Gilson, J., Roemmich, D., 2017. An Argo mixed layer climatology and datasbase. Geophys. Res. Lett. 44, 5618–5626.

Hong, S.Y., Pan, H.L., 1996. Nonlocal boundary layer vertical diffusion in a medium-range forecast model. Mon. Weather Rev. 124 (10), 2322–2339.

Huffman, G.J., Bolvin, D.T., Nelkin, E.J., Tan, J., 2019. Integrated multi-satellitE retrievals for GPM (IMERG) technical documentation. Nasa/Gsfc Code 612 (47), 2019.

IMERG, 2022: ⟨https://gpm.nasa.gov/data/directory⟩.

Jayasankar, C.B., Misra, V., Karmakar, N., 2023. A comparative study between regional atmospheric model simulations coupled and uncoupled to a regional ocean model of the Indian summer monsoon. Earth Space Sci. 10, e2022EA002733. https://doi.org/10.1029/2022EA002733.

Kain, J., Fritsch, M., 1993. Convective parameterization for mesoscale models: the Kain-Fritsch scheme. Meteorol. Monogr. 24, 165–170.

Kanamitsu, M., Ebusuzaki, W., Woollen, J., et al., 2002. NCEP-DOE AMIP-II reanalysis (R-2). Bull. Am. Meteorol. Soc. 83, 1631–1643. https://doi.org/10.1175/bams-83-11- 1631(2002)0832.3.co;2.

Kimutai, J., Barnes, C., Zachariah, M., Clarke, B., Pinto, I., Wolski, P., Stewart, S., Vahlberg, M., Banthiya, A., Thalheimer, L., Otto, F.E.L., 2023. Compounding natural hazards and high vulnerability led to severe impacts from Horn of Africa flooding exacerbated by climate change and Indian Ocean Dipole. World Weather Attribution. Imperial College London. https://doi.org/10.25561/108015.

Kinuthia, J.H., 1992. Horizontal and vertical structure of the Lake Turkana jet. J. Appl. Meteorol. 31 (11), 1248–1274. https://doi.org/10.1175/1520-0450 (1992)0312.0.CO;2.

Kinuthia, J.H., Asnani, G.C., 1982. A newly found jet in North Kenya (Turkana Channel). Mon. Weather Rev. 110 (11), 1722–1728. https://doi.org/10.1175/1520-0493(1982)1102.0.CO;2.

Krishnamurti, T.N., Subramaniam, M., Oosterhof, D.K., Daughenbaugh, G., 1990. Predictability of low frequency modes. Meteorol. Atmos. Phys. 44, 63–83.

Large, W.G., McWilliams, J.C., Doney, S.C., 1994. Oceanic vertical mixing: a review and a model with a nonlocal boundary layer parameterization. Rev. Geophys. 32 (4), 363–403.

Li, H., Misra, V., 2014. Thirty-two-year ocean–atmosphere coupled downscaling of global reanalysis over the IntraAmerican Seas. Clim. Dyn. 43, 2471–2489. https://doi.org/10.1007/s00382-014-2069-9.

Liu, W., Cook, K.H., Vizy, E.K., 2020. Influence of Indian Ocean SST regionality on the East African short rains. Clim. Dyn. 54, 4991–5011. https://doi.org/10.1007/s00382-020-05265-8.

Lyon, B., 2014. Seasonal drought in the Greater Horn of Africa and its recent increase during the March–May long rains. J. Clim. 27 (21), 7953–7975.

Mellor, G.L., Yamada, T., 1982. Development of a turbulence closure model for geophysical fluid problems. Rev. Geophys. 20 (4), 851–875.

Misra, V., 2003. The influence of Pacific SST on the precipitation over southern Africa diagnosed from an AGCM. J. Climate 16, 2408–2418.

Misra, V., Jayasankar, C.B., Mishra, A.K., Mitra, A., Murgavel, P., 2022. Dynamic downscaling the South Asian summer monsoon from a global reanalysis using a regional coupled ocean-atmosphere model J. Geophys. Res 127, e2022JD037490. https://doi.org/10.1029/2022JD037490.

Misra, V., Jayasankar, C.B., 2022. A high resolution coupled ocean-atmosphere simulation of the regional climate over Central America. Clim. Dyn. https://doi.org/10.1007/s00382-021-06083-2.

Misra, V., Jayasankar, C.B., 2023. Characterizing the Madden-Julian Oscillation in the western Pacific Ocean from a regional coupled ocean-atmosphere model simulation Quart. Roy. Met. Soc. https://doi.org/10.1002/qj.4620.

Monteguet, C.B., Madec, G., Fishcher, A.S., Lazar, A., Ludicone, D., 2004. Mixed layer depth over the global ocean: an examination of profile data and a profile-based climatology. J. Geophys. Res. 109, C12003. https://doi.org/10.1029/2004JC002378.

Nicholson, S.E., 1996. A review of climate dynamics and climate vari- ability in Eastern Africa. In: Johnson, T.C., Odada, E. (Eds.), The limnology, climatology and paleoclimatology of the East African lakes. Gordon and Breach, Amsterdam, pp. 25–56.

Nicholson, S.E., 2011. Dryland Climatology. Cambridge Univ. Press, New York, p. 516.

Nicholson, S.E., 2017. Climate and climatic variability of rainfall over eastern Africa. Rev. Geophys. 55, 590–635. https://doi.org/10.1002/2016RG000544.

Nicholson, S.E., Entekhabi, D., 1986. The quasi-periodic behavior of rainfall variahility in Africa and itsrelationship tothe SouthernOscillation. J. Clim. Appl. Meteorol. 34, 311–348.

Nyamweya, C., Desjardins, C., Sigurdsson, S., Tomasson, T., Taabu-Munyaho, A., Sitoki, L., et al., 2016. Simulation of Lake Victoria circulation patterns using the Regional Ocean Modeling System (ROMS). PLoS ONE 11 (3), e0151272. https://doi.org/10.1371/journal.pone.0151272.

Ogwang, B.A., Chen, H., Li, X., Gao, C., 2016. Evaluation of the capability of RegCM4.0 in simulating East African climate. Theor. Appl. Clim. 124 (1–2), 303–313. https://doi.org/10.1007/s00704-015-1420-3.

Paegle, J., Geisler, J.E., 1986. The effect of East African topography on flow driven by zonally symmetric forcing. J. Atmos. Sci. 43 (17), 1862–1872. https://doi.org/10.1175/1520-0469(1986)043< 1862:TEOEAT> 2.0.CO;2.

Palmer, P.I., Wainwright, C.M., Dong, B., Maidment, R.I., Wheeler, K.G., coauthors, 2023. Drivers and impacts of Eastern African rainfall variability. Nat. Rev., Earth Environ. https://doi.org/10.1038/s43017-023-00397-x.

PSL, 2022: ⟨https://psl.noaa.gov/data/gridded/data.ncep.reanalysis2.html⟩.

Raymond, D.J., 2000. Thermodynamic control of tropical rainfall. Q J. R. Meteor. Soc. 126, 889–898. https://doi.org/10.1002/qj.49712.656406.

Reynolds, R.W., Smith, T.M., Liu, C., Chelton, D.B., Casey, K.S., Schlax, M.G., 2007. Daily high-resolution-blended analyses for sea surface temperature. J. Clim. 20, 5473–5496. https://doi.org/10.1175/JCLI-D-14-00293.1.

Shchepetkin, A.F., McWilliams, J.C., 2005. The regional oceanic modeling system (ROMS): a split-explicit, free-surface, topography-following-coordinate oceanic model. Ocean Model. 9 (4), 347–404.

Slingo, J., Spencer, H., Hoskins, B., Berrisford, P., Black, E., 2005. The meteorology of the western Indian Ocean, and the influence of the East African highlands. Philos. Trans. A Math. Phys. Eng. Sci. 363 (1826), 25–42. https://doi.org/10.1098/rsta.2004.1473.

SODA, 2022: ⟨https://iridl.ldeo.columbia.edu/SOURCES/.CARTON-GIESE/.SODA/.v2p2p4/?Set-Language=en⟩.

Sun, Liqiang, Semazzi, Fredrick, H.M., Giorgi, Filippo, Ogallo, Laban, 1999. Application of the NCAR regional climate model to eastern Africa: simulation of the short rains of 1988. J. Geophys. Res. Atmos. 104 (D6), 6529–6548.

Sun, X., Xie, L., Semazzi, F.H.M., Liu, B., 2015. Effect of Lake surface temperature on the spatial distribution and intensity of the precipitation over the Lake Victoria Basin. Mon. Weather Rev. 143 (4), 1179–1192. https://doi.org/10.1175/Mwr-D-14-00049.1.

Thiery, W., Davin, E.L., Panitz, H.J., Demuzere, M., Lhermitte, S., Van Lipzig, N.P.M., 2015. The impact of the African Great Lakes on the regional climate. J. Clim. 28 (10), 4061–4085. https://doi.org/10.1175/JCLI-D-14-00565.1.

Tiedtke, M., 1983. The sensitivity of the time-mean large-scale flow to cumulus convection in the ECMWF model. In: Proceedings of the ECMWF Workshop on Convective in Large-scale Models. European Centre for Medium-Range Weather Forecasts, Reading, United Kingdom 297–316.

UCAR, 2022: ⟨https://rda.ucar.edu/datasets/ds091.0/⟩.

Umlauf, L., Burchard, H., 2003. A generic length-scale equation for geophysical turbulence models. J. Mar. Res. 61 (2), 235–265.

Ummenhofer, C.C., Sen Gupta, A., England, M.H., Reason, C.J.C., 2009. Contributions of Indian Ocean sea surface temperatures to enhanced East African rainfall. J. Clim. 22, 993–1013. https://doi.org/10.1175/2008JCLI2493.1.

Van de Walle, J., Thiery, W., Brousse, O., Souverijns, N., Demuzere, M., van Lizpig, N.P.M., 2020. A convection-permitting model for the Lake Victoria Basin: evaluation and insight into the mesoscale versus synoptic atmospheric dynamics. Clim. Dyn. 54, 1779–1799.

Vizy, Edward K., Cook, Kerry H., 2019. Observed relationship between the Turkana low-level jet and boreal summer convection. Clim. Dyn. 53 (7–8), 4037–4058.

Yang, W., Seager, R., Cane, M.A., Lyon, B., 2015. The annual cycle of East African Precipitation. J. Clim. 28, 2385–2404.

Yasunaga, K., Mapes, B.E., 2012. Differences between more-divergent vs. more-rotational types of convectively coupled equatorial waves. Part I: space–time spectral analyses. J. Atmos. Sci. 69, 3–16. Available from: https://doi. org/10.1175/JAS-D-11-033.1.

Yin, X., Nicholson, S.E., Ba, M.B., 2000. On the diurnal cycle of cloudiness over Lake Victoria and its influence on evaporation from the lake. Hydrol. Sci. J. 45 (3), 407–424. https://doi.org/10.1080/026266600094923.

Yin, X.G., Nicholson, S.E., 1998. The water balance of Lake Victoria. Hydrol. Sci. J. 43 (5), 789–811. https://doi.org/10.1080/026266698094921.

Zhao, Q., Carr, F.H., 1997. A prognostic cloud scheme for operational NWP models. Mon. Weather Rev. 125 (8), 1931–1953.